

pubs.acs.org/JACS Article

"Atomic Topping" of MnO_x on Al_2O_3 to Create Electron-Rich, Aperiodic, Lattice Oxygens that Resemble Noble Metals for Catalytic Oxidation

Tao Gan, Xin Chen, Xuefeng Chu, Pei Jing, Shaozhen Shi, Zedong Zhang, Wenxiang Zhang, Jiong Li, Shuo Zhang, Michele Pavanello, Dayang Wang, and Gang Liu



Cite This: J. Am. Chem. Soc. 2024, 146, 16549–16557



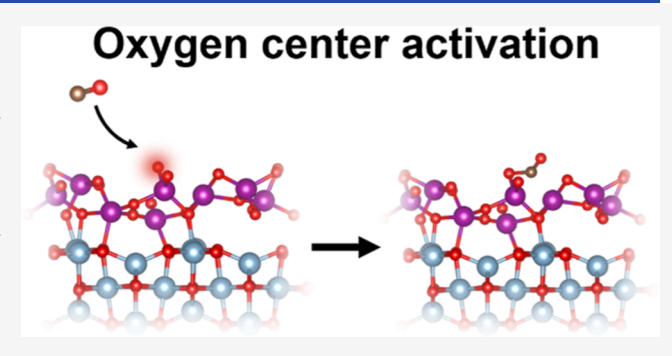
ACCESS I

III Metrics & More

Article Recommendations

Supporting Information

ABSTRACT: Enhancing the catalytic oxidation activity of traditional transition-metal oxides to rival that of noble metals has been a prominent focus in the field of catalysis. However, existing synthesis strategies that focus on controlling the electronic states of metal centers have not yet fully succeeded in achieving this goal. Our current research reveals that manipulating the electronic states of oxygen centers can yield unexpected results. By creating electron-rich, aperiodic lattice oxygens through atomic topping of MnO_x , we have produced a catalyst with performance that closely resembles supported Pt. Spherical aberration-corrected transmission electron microscopy and X-ray absorption spectra have confirmed that the atomic topping of the MnO_x layer on Al_2O_3 can



form an aperiodic arrangement oxide structure. Near-ambient pressure X-ray photoelectron spectroscopy, in situ diffuse reflectance infrared Fourier transform spectroscopy, reaction kinetics test, and theoretical calculations demonstrated that this structure significantly increases the electron density around the oxygen in MnO_x, shifting the activation center for CO adsorption from Mn to O, thereby exhibiting catalytic activity and stability close to that of the precious metal Pt. This study presents a fresh perspective on designing efficient oxide catalysts by targeting electron-rich anionic centers, thereby deepening the understanding of how these centers can be altered to enhance catalytic efficiency in oxidation reactions.

■ INTRODUCTION

The catalytic oxidation reaction using molecular oxygen as the oxygen source is an important reaction process in heterogeneous catalysis, widely used in fields such as gas pollutant elimination and fine chemical synthesis. 1-8 Earth-abundant transition-metal oxides, in comparison with precious metals, have sparked interest in research and development of oxidation catalysts because of their low-cost and biological relevance. However, the development of metal oxide catalysts guided by the metal-centered redox mechanism (i.e., the Mars-van Krevelen mechanism) often leads to complications related to activity and stability of the catalysts. The established Marsvan Krevelen mechanism for heterogeneously catalyzed oxidation reactions involves adsorption of reactant molecules on metal centers and the transfer of oxygen atoms from a solid oxide to a reactant gas, which requires energy to break bonds and form new bonds. 14-17 The overall process is thermodynamically favorable but kinetically slow. Thus, it requires energy input and modulation of reactive species for improved reaction kinetics.

Finding new reaction pathways to break through metalcentered redox mechanisms is the most promising solution to enhancing catalytic performance. For metal oxide catalysts, it is necessary to consider exploiting the role of lattice oxygen in the activation of reactant adsorption, but this poses significant challenges as it requires significant reactivity enhancement in the electronic properties of lattice oxygen. Although the lattice oxygen-centered redox mechanism has highlighted some critical advantage in the oxygen evolution reaction and NO oxidation, the catalysts (mainly for doped oxide materials) do not exhibit the expected universality for catalytic oxidation reactions. The effectiveness of catalysts is significantly affected by external factors, including the influence of an external electric field on lattice oxygen during oxygen evolution reactions and the importance of the electronegativity of nitrogen in the reactants during NO storage and oxidation processes.

Received: March 6, 2024 Revised: May 23, 2024 Accepted: May 23, 2024 Published: June 7, 2024





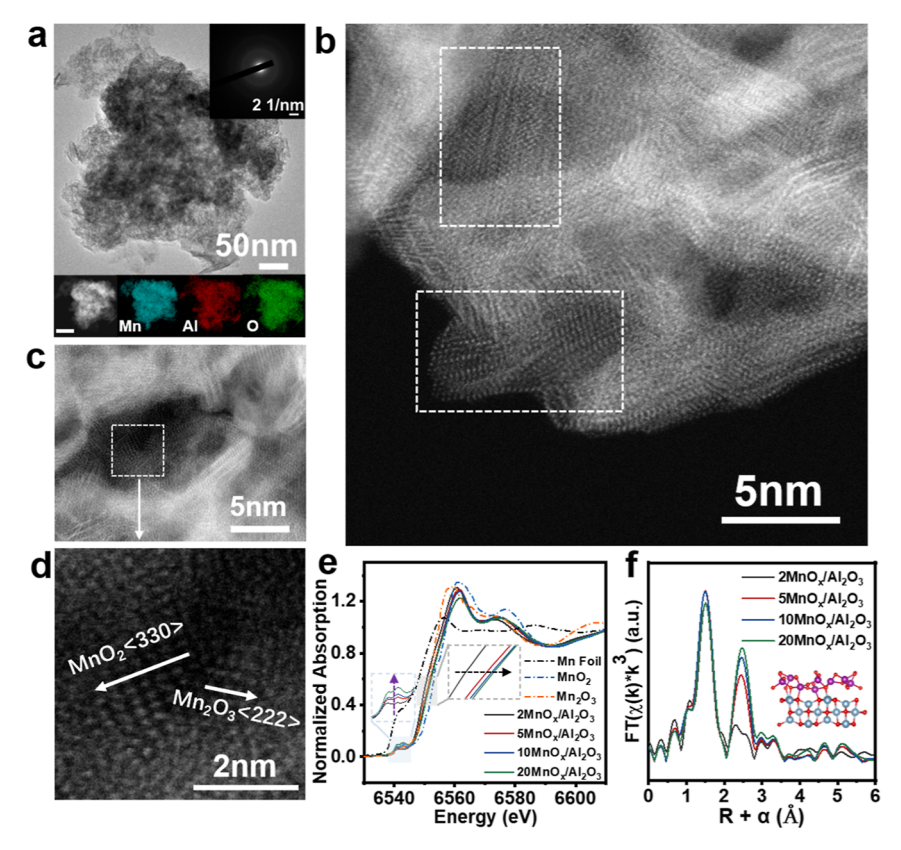


Figure 1. Structure characterization of MnO_x/Al_2O_3 . (a) TEM images of $20MnO_x/Al_2O_3$, inset is the SAED pattern, and below is the EDS element mapping (scale bars, 100 nm). (b,c) AC-TEM images of $20MnO_x/Al_2O_3$. The white rectangular areas show the MnO_x atomic layer. (d) Enlargement of the white rectangular area in (c). (e) XANES results of the Mn K-edge. (f) R-space spectra of different samples.

In recent years, atomically dispersed catalysts with adjustable coordination environment and electronic structure have attracted great interest due to their high atomic utilization efficiency and the unique quantum size effects of nanomaterials. Atomic-layered catalysts with dense active centers can also exhibit synergistic effects between adjacent atoms. Nevertheless, current research efforts primarily concentrate on enhancing the efficiency of noble metals' utilization and exploring the cooperative catalysis between adjacent noble metal atoms. There is still uncertainty about whether oxide materials formed at the atomic level will exhibit special properties and how they might affect the electronic properties of oxygen in the surrounding environment.

In this work, we found that the "atomic topping" MnO_x layer on Al₂O₃ is advantageous in controlling the electronic properties of lattice oxygen. The large area atomically dispersed "manganese layer topping" on the surface of alumina forms an aperiodic structure that significantly increases the electron density around the oxygen in MnO_x. Complementary characterization, including near-ambient pressure X-ray photoelectron spectroscopy (NAP-XPS) and in situ diffuse reflectance infrared Fourier transform spectroscopy (in situ DRIFTS), reaction kinetics test, and theoretical calculations based on DFT have demonstrated that the activation center for CO adsorption effectively shifts from Mn to O, exhibiting catalytic activity and stability close to that of precious metal Pt.

RESULTS AND DISCUSSION

Synthesis and Characterization of MnO_x/Al₂O₃ Catalysts. MnO_x/Al₂O₃ materials were prepared by in situ reduction of KMnO₄ loaded on the surface of γ -Al₂O₃ using

H₂O₂ as the reducing agent (experimental details are shown in the Supporting Information, Figure S1). The obtained manganese oxide species were uniformly dispersed on the surface of alumina, and no crystalline large particles were detected, which was confirmed by XRD, EDS elemental mapping, TEM, and nitrogen adsorption isotherms (Figures 1a, S2, and S4, and Table S1). Spherical aberration-corrected transmission electron microscopy (AC-TEM, Figure 1b-d) was employed to analyze the microstructure of surface Mn species. The two-dimensional structure of manganese oxide presents an aperiodic state spread on the surface of γ -Al₂O₃, and lattice stripes belonging to MnO2 and Mn2O3 can be clearly observed in the adjacent region (Figure 1d). This phenomenon can be observed in all the detected regions of the MnO_x/Al₂O₃ sample with a 20% Mn content (Figures 1b and S5). X-ray absorption near edge structure (XANES) further confirms the aperiodic state of manganese oxide (Figure 1e). With the increase of manganese content, the intensity of preedge peak increased (the blue rectangular area and purple arrow), reflecting the gradual reduction of material symmetry.31 In addition, the blue shift of absorption-edge band edge (the gray rectangular area and black arrow) with the increase of Mn content implies that the Mn valence state increased and 3d orbital occupancy decreased.³²

Fourier transform (FT) of the extended X-ray absorption fine structure (EXAFS) spectra (Figure 1f) of the MnO_x/Al₂O₃ shows that all these samples exhibit a prominent peak at 1.49 Å that corresponds to the first shell of Mn–O coordination, while the peak at 2.46 Å is associated with the second shell of Mn–O–Mn coordination. Quantitative FT-EXAFS fitting results (Figure S6 and Table S2) show that all these samples

are with similar Mn–O coordination number of about 3.5 and gradually increasing Mn–O–Mn contribution from 0.9 of $2MnO_x/Al_2O_3$ to 2.9 of $20MnO_x/Al_2O_3$. At the same time, the bond length of Mn–O increases with the increase in Mn content (Figure S7 and Table S2), which is correlated with the Mn valence state information reflected by XANES, indicating that the covalent electrons between Mn and O are more likely to be distributed around O.

Mn 2p, Mn 3s (Figure S8), and O 1s (Figure S9) XPS results further validate the results of XANES and EXAFS. The binding energy of Mn 2p increased from 641.7 eV of 2MnO_x/Al₂O₃ to 642.5 eV of 20MnO_x/Al₂O₃ (Figure 2a). The spectral

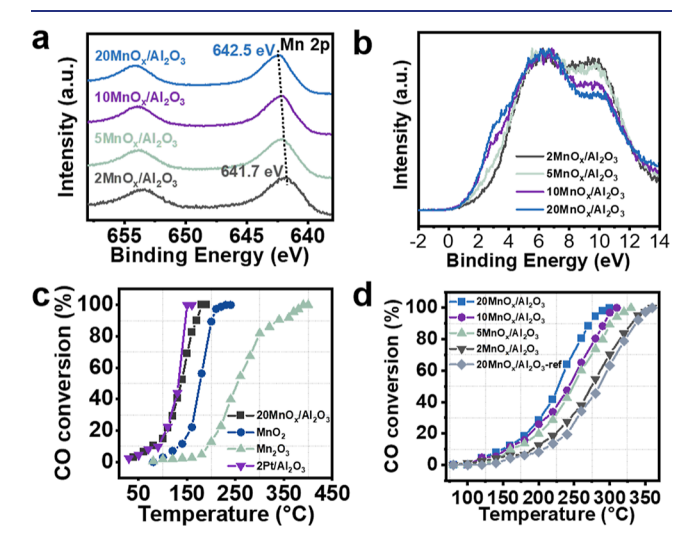


Figure 2. Electronic properties and catalytic activity of different catalysts. (a) Mn 2p XPS results. (b) XPS valence band spectrum. (c) CO conversion curves of different samples. Reaction conditions: SV = $60,000 \text{ mL} \cdot \text{g}^{-1} \cdot \text{h}^{-1}$, 1 vol % CO, 5 vol % O₂, and Ar balanced. (d) CO conversion curves measured by diluting the catalyst with Al₂O₃ to achieve the same Mn content, among which 2MnO_x/Al₂O₃ is not diluted. Other reaction conditions are the same as (c).

splitting of the Mn 3s spectrum decreased with increasing Mn, implying that Mn loses electrons and increases valence (Figure

S8). 33,34 The valence band photoemission spectra of MnO_x/Al₂O₃ are further investigated. Figure 2b shows a significant increase in the intensity around the Fermi energy of MnO_x/Al₂O₃ as Mn content increases. The experimental data and DFT results indicate that the valence band is jointly contributed by Mn and O (Figure S11). Among them, O contributed more significantly, which fully confirms the formation of electron-rich oxygen in $20\text{MnO}_x/\text{Al}_2\text{O}_3$. The electron-rich oxygen exhibits significantly enhanced reactivity, which can be verified by the results of H₂-TPR (Figure S12) and O₂-TPD (Figure S13).

Catalytic Activity Evaluation. Catalytic CO oxidation was first carried out to compare the catalytic performance of MnO_x/Al₂O₃ with different Mn contents. The H₂O₂ treatment increasing the activity of alumina has been ruled out and we only focus on the properties of surface MnO_x layer (Figure S14). CO conversion over these catalysts exhibits S-shaped curves and increases upon the increase of reaction temperature. The samples exhibit activity trend of 20MnO_x/Al₂O₃ > $10\text{MnO}_x/\text{Al}_2\text{O}_3 > 5\text{MnO}_x/\text{Al}_2\text{O}_3 > 2\text{MnO}_x/\text{Al}_2\text{O}_3$ (Figure S15). We also compare the performance of 20MnO_x/Al₂O₃ with representative manganese oxides catalysts, including MnO₂ and Mn₂O₃ (Figure 2c). Among them, 20MnO_x/ Al₂O₃ exhibited the highest activity. Under normal conditions, T_{50} (50% conversion temperature of CO) was achieved at 137 °C, which is about 40 °C lower than that of MnO₂ and 118 °C lower than that of Mn₂O₃. The catalytic performance of 20MnO_x/Al₂O₃ is even comparable with 2 wt % Pt/Al₂O₃ (Figure 2c, $T_{50} = 133$ °C) and higher or comparable in comparison with the supported-Pt catalysts reported in the literatures (Table S3). The catalyst also performs well in the oxidation of toluene. It is known that a great deal of strategies have been carried out to improve the catalytic activity of Mnbased catalysts, such as optimizing crystal phases, creating surface vacancies, and forming heterostructure or bimetallic oxides. The catalytic performance of MnO_x/Al₂O₃ remains comparable or leading among these reported results (Figure S16 and Table S4). All these results showed that constructing atomic-layered structure manganese oxides on the surface of

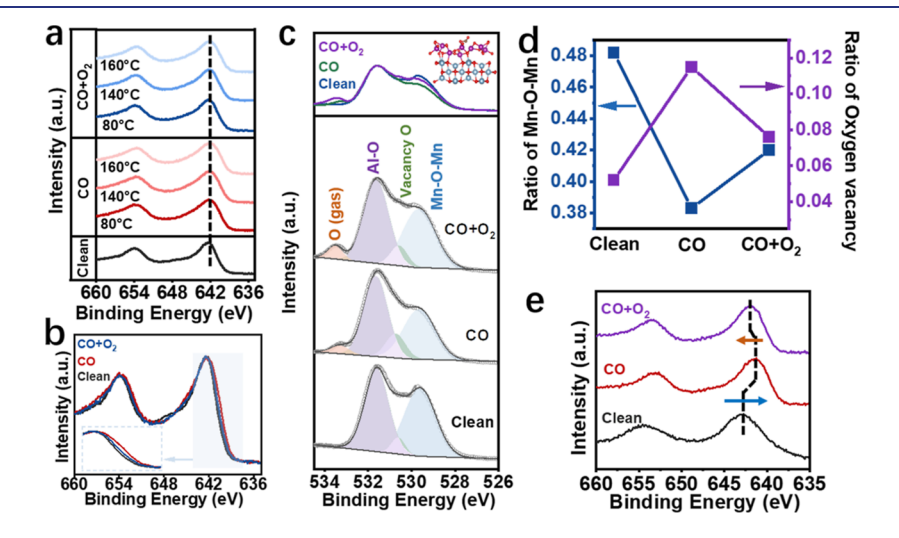


Figure 3. Dynamic changes of catalysts. (a) Mn 2p NAP-XPS of $20\text{MnO}_x/\text{Al}_2\text{O}_3$ at different temperatures and atmospheres. (b) Raw spectrum of Mn 2p NAP-XPS results at 80 °C. (c) Raw spectrum of the O 1s NAP-XPS at 80 °C (top) and deconvolution of the O 1s spectrum based on the peak-fitting parameters at different atmospheres. (d) Ratio changes of different species in different atmospheres based on peak-fitting results. (e) Mn 2p NAP-XPS results of $20\text{MnO}_x/\text{Al}_2\text{O}_3$ -ref under different atmospheres at 160 °C.

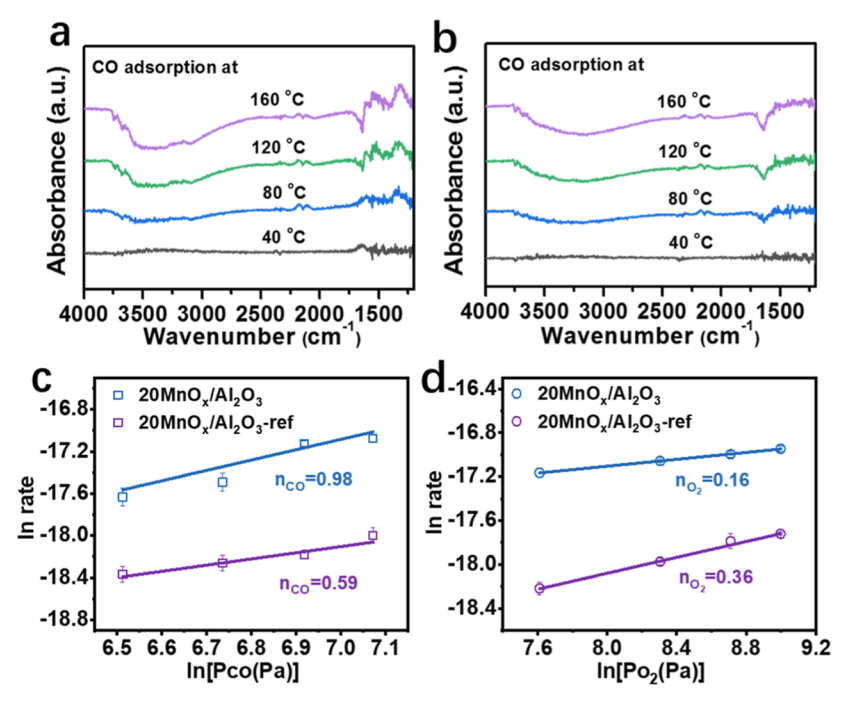


Figure 4. Reaction mechanism analysis. (a,b) In situ DRIFTS of a $20 \text{MnO}_x/\text{Al}_2\text{O}_3$ and (b) $20 \text{MnO}_x/\text{Al}_2\text{O}_3$ -ref under a CO atmosphere at different temperatures. (c,d) Reaction rate as a function of the CO partial pressure (c) or the O_2 partial pressure (d). The error bar represents the standard deviation based on three measurements under a given pressure.

 $\mathrm{Al_2O_3}$ could obtain highly efficient catalysts for catalytic oxidation.

The above test is carried out under the same mass of catalysts, where the amount of Mn is different (Figure S15). To avoid the influence of the Mn content, we also investigate the performance of dilute MnO_x/Al₂O₃ samples with Al₂O₃ to maintain the same amount of Mn sites. Under this reaction condition, the samples exhibit similar activity trend in catalytic CO oxidation, that is, $20MnO_x/Al_2O_3 > 10MnO_x/Al_2O_3 >$ $5MnO_x/Al_2O_3 > 2MnO_x/Al_2O_3$. Combining the characterization results of XANES and XPS, the reaction results suggest that electron-rich oxygen and the high-valence state Mn exhibit high catalytic activity. To confirm this proposition, a type of manganese oxide with a relatively low-valence state of Mn was synthesized. To be comparable with the previous samples, the Mn content was also controlled at 20%, and alumina was used as the support. The characterization results, including XRD, XPS, XANES, EXAFS, and AC-TEM (Figures S18-S24, Table S5), represent that manganese oxide is dispersed on the surface of alumina in the form of nanoparticles of around 10 nm, with an average valence state of Mn of about 2.88. Considering the metal-centered redox mechanism, the low-valence state of Mn should be more favorable for the adsorption and activation of CO. In contrast, 20MnO_x/Al₂O₃-ref exhibits obviously low activity in catalytic oxidation, much lower than that of 20MnO_x/Al₂O₃ (Figure 2d). This result confirms, on one hand, that electron-rich oxygen and high-valence state Mn are more favorable for CO oxidation while also indicating that the catalyst does not follow a metal-centered redox mechanism.

Mechanism Study of MnO_x Atomic Layer in Catalytic CO Oxidation. To observe the structural dynamics of MnO_x two in situ spectroscopy approaches were employed. Among them, in situ NAP-XPS was used to measure the surface electronic properties of the working catalysts and in situ DRIFTS was carried out to probe the interaction of the surface

sites with the reacting molecules. The NAP-XPS spectra of the Mn 2p shown in Figure 3a reveal that the 20MnO_x/Al₂O₃ contains similar Mn states under clean, CO, and CO + O₂ conditions at different temperatures. There is no evidence to suggest that direct interaction exists between Mn sites and reactants. When we zoom the peak edge of Mn 2p XPS, we can observe some subtle changes (Figure 3b). The Mn 2p signal moves toward low binding energy as CO introduces and partially restores with the addition of oxygen. These subtle changes should be caused by the charge disturbance of the neighboring atoms. The obvious change can be measured in the O 1s XPS spectra of $20\text{MnO}_x/\text{Al}_2\text{O}_3$ (Figure 3c). The ratio of Mn-O-Mn (at 529.7 eV) decreased from 0.482 at the clean state to 0.383 at a CO atmosphere, which means that the active bridge lattice oxygen was consumed by CO. DFT simulations indicate that CO tends to adsorb on the O sites to initiate the reaction. Meanwhile, the oxygen vacancy (at 530.6 eV) increased from 0.052 to 0.115. The peak at 531.6 eV remaining almost unchanged means that Al-O is inert.

After introducing O2, the consumed Mn-O-Mn signal is partially restored to 0.420 and oxygen vacancy is decreased to 0.076 (Figure 3d). This implies that oxygen backfilling and Mn-O-Mn centers recover. When the temperature was changed to 140 and 160 °C in a CO atmosphere, Mn-O-Mn species decreased and formed oxygen vacancies, which means that the reaction further proceeds as the temperature increases (Figure S25a,c,e). After adding O_2 , the above two signals show opposite changes. The Mn-O-Mn species increased and oxygen vacancy decreased as temperature rising implies oxygen backfill (Figure S25b,d,f). However, we can find that the CO atmosphere shows more steeper curves than the CO + O₂ atmosphere, which means that the catalytic cycle can operate well at 80 °C and O2 can be well activated even at lower temperature. This reaction pathway shows a new Mars-van Krevelen mechanism led by exposed oxygen sites instead of the

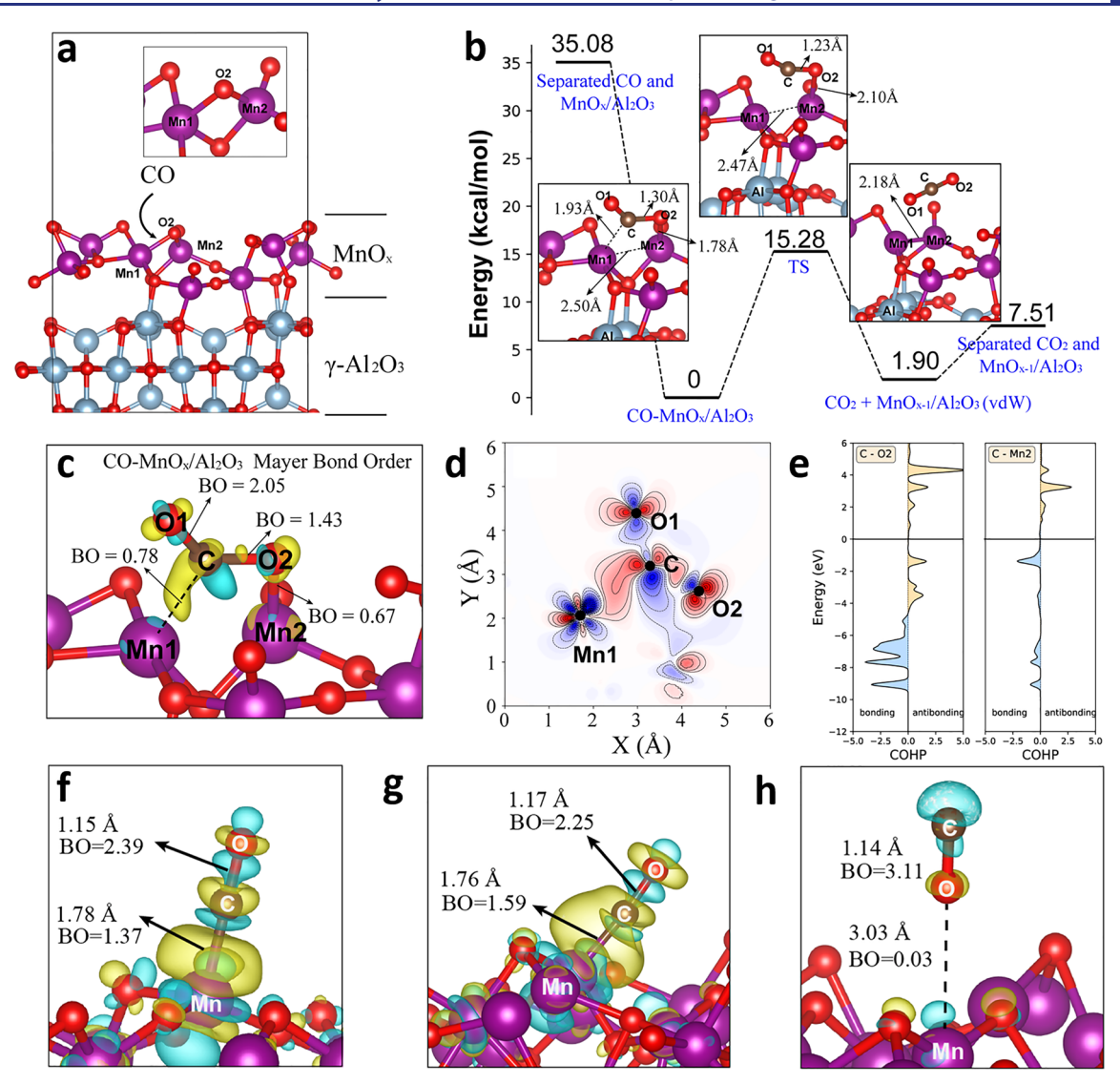


Figure 5. DFT calculation results. (a) Optimized structure of MnO_x/Al₂O₃, with atoms Mn1, Mn2, and O2 labeled that they are involved in the reaction. The arrow indicates the site at which CO is adsorbed. (b) As the reaction pathway from CO to CO₂, the DFT energy of adsorption structure CO–MnO_x/Al₂O₃ is set to zero as reference. The reactant (CO–MnO_x/Al₂O₃), transition state, and product (vdW complex of CO₂ with MnO_x/Al₂O₃) structures are presented along with the energy profile. (c) Enlarged detailed structure plot includes electron density difference (isosurface value: 0.03 e/Å³) of CO–MnO_x/Al₂O₃ and Mayer bond orders (BO) are also labeled on the bonds. (d) Electron density difference contour plot of CO–MnO_x/Al₂O₃, the contour plane is defined by three Mn1, C, and O2 atoms; the red regions indicate electron accumulation and the blue regions indicate electron decrease. (e) Projected COHP on the C–O2 and C–Mn2 bonds. Fermi energy is set at 0 eV. (f) CO adsorption on the α-Mn₂O₃(001) surface, isovalue: (isosurface value: 0.05 e/Å³); (g) CO adsorption on the α-Mn₂O₃(110) surface, isovalue: (isosurface value: 0.01 e/Å³). The Mayer bond order and bond length are labeled.

metal center. We also performed the reference experiment, the corresponding NAP-XPS spectra for the $20 \mathrm{MnO}_x/\mathrm{Al}_2\mathrm{O}_3$ -ref sample exhibit three different states of Mn under similar conditions (Figure 3e). Obviously, the Mn chemical states of $20 \mathrm{MnO}_x/\mathrm{Al}_2\mathrm{O}_3$ -ref are dependent on the applied reaction conditions, suggesting the presence of interaction between CO and the cationic Mn site. Such an interaction includes the electrostatic, σ , and π contributions to the bonding of CO in M^{n+} –CO species. Among them, π -back-donation from CO causes the negative shift of Mn 2p binding energy. The copresence of CO and O₂ weakens this negative shift due to the increase of CO_2 formation rate in the oxygen atmosphere. Based on these results, we can preliminarily propose that CO oxidation over $20 \mathrm{MnO}_x/\mathrm{Al}_2\mathrm{O}_3$ -ref should mainly proceed via the conventional Mars—van Krevelen mechanism.

Using CO as a probe molecule, the interaction of the surface sites with the reacting molecules was further measured by in situ DRIFTS (Figure 4a,b). The samples were first pretreated in an Ar flow (20 mL min $^{-1}$) at 200 °C for 20 min to remove the adsorbed water and molecular oxygen. The spectra of the pretreated samples were recorded as backgrounds. Generally, $3800-3000~\rm cm^{-1}$ is the stretching region of O–H. Among them, bands at 3710-3700, 3660-3640, and $3550-3500~\rm cm^{-1}$ are assigned to isolated hydroxyls, bridging hydroxyls, and multiple bonded hydroxyls, respectively. The broad band at $3400-3100~\rm cm^{-1}$ can be ascribed to the hydrogen-bridging hydroxyls. In our case, broad negative peaks can be observed over two representative samples, $20 \rm MnO_x/Al_2O_3$ and $20 \rm MnO_x/Al_2O_3$ -ref, indicating the formation of $-\rm OH-CO$ complexes (the formate species) during the CO adsorption. In

this region, 20MnO_x/Al₂O₃ has no significant difference with 20MnO_x/Al₂O₃-ref because of the presence of large amount of Mn-OH and Al-OH on the surface of two samples. The OH groups can easily react with CO to form the formate species, even at low temperatures. The difference is located in the region of 1700-1200 cm⁻¹. Such signals can be readily assigned to the C-O stretching and bending modes of carbonate and formate species. In this region, very weak signals can be observed over 20MnO_x/Al₂O₃-ref. On the contrary, the apparent peaks of 20MnO_x/Al₂O₃ at 1606, 1541, and 1324 cm⁻¹ indicate the formation of carbonate species.³⁶ In combination with in situ NAP-XPS and in situ DRIFTS, it can be proposed that CO oxidation occurs through different routes over MnO_x with different surface oxygen activity. Over 20MnO_x/Al₂O₃, CO adsorbed on active O species forms carbonate intermediates, which are easily decomposed into CO₂ during the reaction. While over 20MnO_x/Al₂O₃-ref, the CO adsorbed on metal ions react with the adjacent oxygen species to form CO₂ and complete the oxidation process.

On 20MnO_x/Al₂O₃ samples, the measured CO and O₂ reaction orders were 0.98 and 0.16, respectively. On 20MnO_x/ Al₂O₃-ref samples, the measured CO and O₂ reaction orders were 0.59 and 0.36, respectively (Figure 4c,d). The higher reaction orders of CO than O2 on both catalysts means that O2 adsorption is better than CO. This is consistent with the Mars-van Krevelen mechanism that lattice oxygen acts as the intermediate for oxygen activation and accelerates the reaction rate. 20MnO_x/Al₂O₃ owns higher CO reaction order and lower O₂ reaction order than 20MnO_x/Al₂O₃-ref. It indicates that $20MnO_x/Al_2O_3$ has a facile oxygen activation and low CO coverage than $20MnO_x/Al_2O_3$ -ref. As proved by NAP-XPS, 20MnO_x/Al₂O₃-ref with low-valence Mn centers can absorb CO easily. This may be the reason for the high CO coverage on 20MnO_x/Al₂O₃-ref. As for 20MnO_x/Al₂O₃, CO prefers to adsorb on the oxygen sites than the Mn centers. The higher surface oxygen activity finally improves the catalytic

DFT calculations were used to further illustrate the reaction mechanism of oxidation of CO to CO₂. CP2K (version 2023.1)³⁹ and Quantum ESPRESSO (v.7.1)^{40,41} are used for DFT calculations. Multiwfn $[3.8(\text{dev})]^{42}$ and LOBSTER $(5.0.0)^{43}$ are used for electron structure analysis. VESTA (Ver. 4.5.8)⁴⁴ is used for visualization. In the construction of the MnO_x/Al₂O₃ substrate model, a monolayer of MnO_x was deposited onto the Al₂O₃ surface. Geometry optimization revealed that the MnO_x layer adheres to the Al₂O₃ substrate through Al-O and Mn-O bonds. The monolayer of MnO_x adopts an amorphous configuration, as shown in Figure 5a, the O atoms are exposed outward, while most of the Mn atoms are enveloped by O atoms. This configuration increases the likelihood of contact between the O atoms in the MnO_x monolayer and CO molecules, compared with the Mn atom. Furthermore, in our analysis of the density of states (DOS, Figure S11), we observed that MnO_x/Al₂O₃ displays a metallic characteristic, primarily attributed to the deposited MnO_x layer that aligns with previous DFT studies on MnO_x surfaces (Mn₂O₃ and Mn₃O₄).

The reaction pathway is depicted in Figure 5b. The CO molecule on MnO_x/Al₂O₃ begins with an adsorption structure where a CO molecule inserts into the bond between O2 and Mn1. O2 acts as a bridging atom linking Mn1 and Mn2 atoms (O1, O2, and Mn2, see Figure 5a). The adsorption energy (defined as the DFT energy of optimized CO–MnO_x/Al₂O₃

minus the DFT energy of optimized isolated CO and isolated MnO_x/Al_2O_3) is -35.08 kcal/mol, indicating a chemical adsorption. The chemical bond properties of the adsorption structure (Figure 5c) have been further researched through electron density difference, the Mayer bond order, 46,47 and crystal orbital Hamilton population (COHP) analysis. 48,49 The bond length between the C and the O2 atoms is 1.30 Å, while the Mn1-C distance is 1.93 Å. Mayer bond orders are also labeled on the detailed adsorption structure in Figure 5c. The larger bond order between C and O2 (1.43) compared to C and Mn1 (0.78) suggests that the C atom in CO exhibits greater affinity toward the O atom. Figure 5d shows the contour plot of the electron density difference ($ho_{\rm CO+bulk} -
ho_{\rm CO}$ $-\rho_{\text{bulk}}$) resulting from the adsorption. The lone pair electrons on the C atom side decrease, while the region between Mn1 and C exhibits electron density accumulation, consistent with the 0.78 bond order of the C-Mn1 bond. COHP in Figure 5e further shows that the bonding orbitals between C and O2 are located in the lower energy region (-10 to -5 eV), whereas the most significant bonding orbital between C-Mn1 is situated much closer to the Fermi level, around -1.6 eV. COHP further proves that the C atom in the CO molecule tends to bind more strongly to the O atom. The weaker interaction between Mn1 and the C atom is crucial for the formation of CO₂ on the MnO_x/Al₂O₃ surface as it requires less activation energy to break the C-Mn bond. The adsorption structure crosses a small transition state barrier of 15.28 kcal/mol and yields a van der Waals (vdW) noncovalent complex of CO_2 and a MnO_{x-1}/Al_2O_3 surface with bimetallic centers (Mn1-Mn2). The desorption energy of the CO₂ molecule from the surface is only 5.61 kcal/mol. The active bimetallic center is exposed to an environment rich in O2 molecules and becomes the next catalytic center. We also calculated the adsorption energies of O2 and CO on the bimetallic center. Our results indicate that O₂ exhibits greater stability in adsorption on the bimetallic center compared to that of CO (Figure S26). Subsequently, in the following reactions, an O2 molecule is adsorbed onto the bimetallic center and oxidizes a CO molecule, and finally, the MnO_x/ Al_2O_3 returns to its original configuration (Figure 5a), through an isomerization reaction (Figure S27). These processes are detailed in Supporting Information, Figure S28, depicting the catalytic cycle.

Afterward, MnO_x/Al_2O_3 -ref used α - Mn_2O_3 as the model because the XRD results displayed its corresponding diffraction peaks (Figure S18). The (001) and (110) surfaces were selected as references. The (001) surface is rich in oxygen atoms, indicating potentially high oxidizing capacity. 50 For completeness, we also selected the (110) surface as a model that exposes both Mn and O atoms. In the studied (001) α -Mn₂O₃ surface, we observed greater surface regularity compared to the MnO₂/Al₂O₃ (comparison in Figure S29). All oxygen atoms act as bridge atoms linking the Mn atoms. In the search for CO adsorption configurations, we employed two initial guess structures: one with the C atom on an O atom on the surface and another with the C atom inserted into the O-Mn bond. Only one stable adsorption configuration was obtained, where the C atom of CO is fully bonded to the Mn atom (Figure 5f), with a binding energy of -37.65 kcal/mol. Different with reactions on the MnO_x/Al₂O₃ surface, the direct reaction paths for CO oxidation to CO₂ by the (001) surface are not feasible without C atom interaction with O atoms on the surface. The (110) surface has similar results, we used

three initial guess geometries to seek the adsorption structures (illustrated in Figure S30), we found an adsorption structure of the C atom bonded on the Mn atom (Figure 5g) and a weak-interaction absorption configuration, wherein the oxygen atom is oriented toward the (110) surface (Figure 5h). The C–Mn bonds on (110) and (001) surfaces are also characterized by the Mayer bond order (labeled in Figure 5). Notably, the finding of C–Mn bonds aligns with the XPS results in Figure 3e.

CONCLUSION

In this study, we manipulated the properties of oxygen species by regulating the atomic arrangement of Mn. The atomic layer of MnO_x distributed on Al₂O₃ was prepared successfully by using a two-step deposition-reduction method. The formed large-area Mn-O-Mn layer structure changes the properties of the bridge lattice oxygen, forming electron-rich oxygen centers. The exposed activated oxygen species on the surface can easily adsorb and activate the CO molecules. Unlike the conventional Mars-van Krevelen mechanism triggered by metal centers, the activation mechanism in the proposed catalyst centers around oxygen sites and exhibits superior reactivity. This work indicates that the properties of active centers can be adjusted by precisely regulating the catalyst structure at the atomic layer level. The MnO_x atomic layer on Al₂O₃ can achieve improved performance in catalytic oxidation compared to conventional manganese oxides through and beyond the performance of the Mars-van Krevelen mechanism.

ASSOCIATED CONTENT

Supporting Information

The Supporting Information is available free of charge at https://pubs.acs.org/doi/10.1021/jacs.4c03299.

Detailed experimental and methods section, other supporting results, catalyst characterization, kinetics analysis, reaction performance, mechanism study, and DFT calculations (PDF)

AUTHOR INFORMATION

Corresponding Authors

Gang Liu — State Key Laboratory of Inorganic Synthesis and Preparative Chemistry, College of Chemistry, Jilin University, Changchun 130012, China; ⊚ orcid.org/0000-0001-9800-0380; Email: lgang@jlu.edu.cn

Michele Pavanello — Department of Chemistry, Department of Physics, Rutgers University, Newark, New Jersey 07102, United States; oorcid.org/0000-0001-8294-7481; Email: m.pavanello@rutgers.edu

Xuefeng Chu – Jilin Provincial Key Laboratory of Architectural Electricity & Comprehensive Energy Saving, School of Electrical and Electronic Information Engineering, Jilin Jianzhu University, Changchun 130118, China; Email: stone2009@126.com

Authors

Tao Gan – State Key Laboratory of Inorganic Synthesis and Preparative Chemistry, College of Chemistry, Jilin University, Changchun 130012, China; Shanghai Synchrotron Radiation Facility, Shanghai Advanced Research Institute, Chinese Academy of Sciences, Shanghai 201204, China

- Xin Chen Department of Chemistry, Department of Physics, Rutgers University, Newark, New Jersey 07102, United States; orcid.org/0000-0002-5227-1334
- Pei Jing State Key Laboratory of Inorganic Synthesis and Preparative Chemistry, College of Chemistry, Jilin University, Changchun 130012, China
- Shaozhen Shi State Key Laboratory of Inorganic Synthesis and Preparative Chemistry, College of Chemistry, Jilin University, Changchun 130012, China
- **Zedong Zhang** Department of Chemistry, Tsinghua University, Beijing 100084, China
- Wenxiang Zhang State Key Laboratory of Inorganic Synthesis and Preparative Chemistry, College of Chemistry, Jilin University, Changchun 130012, China
- Jiong Li Shanghai Synchrotron Radiation Facility, Shanghai Advanced Research Institute, Chinese Academy of Sciences, Shanghai 201204, China
- Shuo Zhang Shanghai Synchrotron Radiation Facility, Shanghai Advanced Research Institute, Chinese Academy of Sciences, Shanghai 201204, China
- Dayang Wang State Key Laboratory of Inorganic Synthesis and Preparative Chemistry, College of Chemistry, Jilin University, Changchun 130012, China; orcid.org/0000-0003-3678-6677

Complete contact information is available at: https://pubs.acs.org/10.1021/jacs.4c03299

Author Contributions

[#]T.G. and X.C. contributed equally to this work.

Notes

The authors declare no competing financial interest.

ACKNOWLEDGMENTS

This work was supported by National Key R&D Program of China (2023YFA1506300), National Natural Science Foundation of China (22072054, 21972053, and 22161132009), the Jilin Scientific and Technological Development Program (20230101050JC), Scientific Research Project of Jilin Provincial Department of Education (JJKH20231126KJ), the China Postdoctoral Science Foundation (2022M721796), and the Open Project of the State Key Laboratory of Inorganic Synthesis and Preparative Chemistry (2024-4). This research used the Hard X-ray Spectroscopy Beamline BL11B at the Shanghai Synchrotron Radiation Facility of Chinese Academy of Sciences. This research was also supported by the National Science Foundation under grant OAC-2321103, CHE-2154760, and ACS-PRF 62555-ND6.

REFERENCES

- (1) Montemore, M. M.; van Spronsen, M. A.; Madix, R. J.; Friend, C. M. O₂ Activation by Metal Surfaces: Implications for Bonding and Reactivity on Heterogeneous Catalysts. *Chem. Rev.* **2018**, *118* (5), 2816–2862.
- (2) Gan, T.; Yang, J.; Morris, D.; Chu, X.; Zhang, P.; Zhang, W.; Zou, Y.; Yan, W.; Wei, S. H.; Liu, G. Electron donation of non-oxide supports boosts O₂ activation on nano-platinum catalysts. *Nat. Commun.* **2021**, *12* (1), 2741.
- (3) Beniya, A.; Higashi, S. Towards dense single-atom catalysts for future automotive applications. *Nat. Catal.* **2019**, 2 (7), 590–602.
- (4) Xie, J.; Li, X.; Guo, J.; Luo, L.; Delgado, J. J.; Martsinovich, N.; Tang, J. Highly selective oxidation of benzene to phenol with air at room temperature promoted by water. *Nat. Commun.* **2023**, *14* (1), 4431.

- (5) Li, X.; Pereira-Hernandez, X. I.; Chen, Y.; Xu, J.; Zhao, J.; Pao, C. W.; Fang, C. Y.; Zeng, J.; Wang, Y.; Gates, B. C.; et al. Functional CeO_x nanoglues for robust atomically dispersed catalysts. *Nature* **2022**, *611* (7935), 284–288.
- (6) Fu, N.; Liang, X.; Wang, X.; Gan, T.; Ye, C.; Li, Z.; Liu, J. C.; Li, Y. Controllable Conversion of Platinum Nanoparticles to Single Atoms in Pt/CeO₂ by Laser Ablation for Efficient CO Oxidation. *J. Am. Chem. Soc.* **2023**, *145* (17), 9540–9547.
- (7) Yang, H.; Wang, X.; Liu, Q.; Huang, A.; Zhang, X.; Yu, Y.; Zhuang, Z.; Li, G.; Li, Y.; Peng, Q.; et al. Heterogeneous Iridium Single-Atom Molecular-like Catalysis for Epoxidation of Ethylene. *J. Am. Chem. Soc.* **2023**, *145* (12), 6658–6670.
- (8) Gan, T.; Chu, X.; Qi, H.; Zhang, W.; Zou, Y.; Yan, W.; Liu, G. Pt/Al₂O₃ with ultralow Pt-loading catalyze toluene oxidation: Promotional synergistic effect of Pt nanoparticles and Al₂O₃ support. *Appl. Catal., B* **2019**, 257, 117943.
- (9) Fang, Y.; Zhang, Q.; Zhang, H.; Li, X.; Chen, W.; Xu, J.; Shen, H.; Yang, J.; Pan, C.; Zhu, Y.; et al. Dual Activation of Molecular Oxygen and Surface Lattice Oxygen in Single Atom Cu₁/TiO₂ Catalyst for CO Oxidation. *Angew. Chem., Int. Ed. Engl.* **2022**, *61* (48), No. e202212273.
- (10) Pan, C.; Wang, C.; Zhao, X.; Xu, P.; Mao, F.; Yang, J.; Zhu, Y.; Yu, R.; Xiao, S.; Fang, Y.; et al. Neighboring sp-Hybridized Carbon Participated Molecular Oxygen Activation on the Interface of Subnanocluster CuO/Graphdiyne. *J. Am. Chem. Soc.* **2022**, *144* (11), 4942–4951.
- (11) Xu, H.; Yan, N.; Qu, Z.; Liu, W.; Mei, J.; Huang, W.; Zhao, S. Gaseous Heterogeneous Catalytic Reactions over Mn-Based Oxides for Environmental Applications: A Critical Review. *Environ. Sci. Technol.* **2017**, *51* (16), 8879–8892.
- (12) Hwang, J.; Rao, R. R.; Giordano, L.; Akkiraju, K.; Wang, X. R.; Crumlin, E. J.; Bluhm, H.; Shao-Horn, Y. Regulating oxygen activity of perovskites to promote NO_x oxidation and reduction kinetics. *Nat. Catal.* **2021**, *4* (8), 663–673.
- (13) Liu, X.; Mi, J.; Shi, L.; Liu, H.; Liu, J.; Ding, Y.; Shi, J.; He, M.; Wang, Z.; Xiong, S.; et al. In Situ Modulation of A-Site Vacancies in LaMnO_{3.15} Perovskite for Surface Lattice Oxygen Activation and Boosted Redox Reactions. *Angew. Chem., Int. Ed. Engl.* **2021**, *60* (51), 26747–26754.
- (14) Mars, P.; van Krevelen, D. W. Oxidations carried out by means of vanadium oxide catalysts. *Chem. Eng. Sci.* **1954**, *3*, 41–59.
- (15) Widmann, D.; Behm, R. J. Activation of Molecular Oxygen and the Nature of the Active Oxygen Species for CO Oxidation on Oxide Supported Au Catalysts. *Acc. Chem. Res.* **2014**, *47* (3), 740–749.
- (16) Son, Y. C.; Makwana, V. D.; Howell, A. R.; Suib, S. L. Efficient, Catalytic, Aerobic Oxidation of Alcohols with Octahedral Molecular Sieves. *Angew. Chem., Int. Ed. Engl.* **2001**, 40 (22), 4280–4283.
- (17) Nie, L.; Mei, D.; Xiong, H.; Peng, B.; Ren, Z.; Hernandez, X. I. P.; DeLaRiva, A.; Wang, M.; Engelhard, M. H.; Kovarik, L.; et al. Activation of surface lattice oxygen in single-atom Pt/CeO₂ for low-temperature CO oxidation. *Science* **2017**, 358 (6369), 1419–1423.
- (18) Wang, Q.; Li, Y.; Serrano-Lotina, A.; Han, W.; Portela, R.; Wang, R.; Banares, M. A.; Yeung, K. L. Operando Investigation of Toluene Oxidation over 1D Pt@CeO₂ Derived from Pt Cluster-Containing MOF. J. Am. Chem. Soc. 2021, 143 (1), 196–205.
- (19) He, Z.; Zhang, J.; Gong, Z.; Lei, H.; Zhou, D.; Zhang, N.; Mai, W.; Zhao, S.; Chen, Y. Activating lattice oxygen in NiFe-based (oxy)hydroxide for water electrolysis. *Nat. Commun.* **2022**, *13* (1), 2.191.
- (20) Wang, X.; Xi, S.; Huang, P.; Du, Y.; Zhong, H.; Wang, Q.; Borgna, A.; Zhang, Y. W.; Wang, Z.; Wang, H.; et al. Pivotal role of reversible NiO_6 geometric conversion in oxygen evolution. *Nature* **2022**, *611* (7937), 702–708.
- (21) Grimaud, A.; Diaz-Morales, O.; Han, B.; Hong, W. T.; Lee, Y. L.; Giordano, L.; Stoerzinger, K. A.; Koper, M. T. M.; Shao-Horn, Y. Activating lattice oxygen redox reactions in metal oxides to catalyse oxygen evolution. *Nat. Chem.* **2017**, *9* (5), 457–465.
- (22) Gan, T.; Wang, D. Atomically dispersed materials: Ideal catalysts in atomic era. *Nano Res.* **2024**, *17* (1), 18–38.

- (23) Zhang, Z.; Wang, J.; Ge, X.; Wang, S.; Li, A.; Li, R.; Shen, J.; Liang, X.; Gan, T.; Han, X.; et al. Mixed Plastics Wastes Upcycling with High-Stability Single-Atom Ru Catalyst. J. Am. Chem. Soc. 2023, 145 (41), 22836–22844.
- (24) Han, L.; Cheng, H.; Liu, W.; Li, H.; Ou, P.; Lin, R.; Wang, H. T.; Pao, C. W.; Head, A. R.; Wang, C. H.; et al. A single-atom library for guided monometallic and concentration-complex multimetallic designs. *Nat. Mater.* **2022**, *21* (6), 681–688.
- (25) Qiao, B.; Wang, A.; Yang, X.; Allard, L. F.; Jiang, Z.; Cui, Y.; Liu, J.; Li, J.; Zhang, T. Single-atom catalysis of CO oxidation using Pt₁/FeO_x. *Nat. Chem.* **2011**, 3 (8), 634–641.
- (26) Zhang, Y. X.; Zhang, S.; Huang, H.; Liu, X.; Li, B.; Lee, Y.; Wang, X.; Bai, Y.; Sun, M.; Wu, Y.; et al. General Synthesis of a Diatomic Catalyst Library via a Macrocyclic Precursor-Mediated Approach. *J. Am. Chem. Soc.* **2023**, *145* (8), 4819–4827.
- (27) Xie, S.; Liu, L.; Lu, Y.; Wang, C.; Cao, S.; Diao, W.; Deng, J.; Tan, W.; Ma, L.; Ehrlich, S. N.; et al. Pt Atomic Single-Layer Catalyst Embedded in Defect-Enriched Ceria for Efficient CO Oxidation. *J. Am. Chem. Soc.* **2022**, *144* (46), 21255–21266.
- (28) Xiong, H.; Kunwar, D.; Jiang, D.; García-Vargas, C. E.; Li, H.; Du, C.; Canning, G.; Pereira-Hernandez, X. I.; Wan, Q.; Lin, S.; et al. Engineering catalyst supports to stabilize PdO_x two-dimensional rafts for water-tolerant methane oxidation. *Nat. Catal.* **2021**, *4* (10), 830–830
- (29) Kwak, J. H.; Hu, J.; Mei, D.; Yi, C.-W.; Kim, D. H.; Peden, C. H. F.; Allard, L. F.; Szanyi, J. Coordinatively Unsaturated Al^{3+} Centers as Binding Sites for Active Catalyst Phases of Platinum on γ -Al $_2O_3$. Science **2009**, 325 (5948), 1670–1673.
- (30) Duan, L.; Hung, C. T.; Wang, J.; Wang, C.; Ma, B.; Zhang, W.; Ma, Y.; Zhao, Z.; Yang, C.; Zhao, T.; et al. Synthesis of Fully Exposed Single-Atom-Layer Metal Clusters on 2D Ordered Mesoporous TiO₂ Nanosheets. *Angew. Chem., Int. Ed. Engl.* **2022**, *61* (43), No. e202211307.
- (31) Luo, K.; Roberts, M. R.; Hao, R.; Guerrini, N.; Pickup, D. M.; Liu, Y. S.; Edstrom, K.; Guo, J.; Chadwick, A. V.; Duda, L. C.; et al. Charge-compensation in 3d-transition-metal-oxide intercalation cathodes through the generation of localized electron holes on oxygen. *Nat. Chem.* **2016**, *8* (7), 684–691.
- (32) Zheng, X.; Yang, J.; Li, P.; Wang, Q.; Wu, J.; Zhang, E.; Chen, S.; Zhuang, Z.; Lai, W.; Dou, S.; et al. Ir-Sn pair-site triggers key oxygen radical intermediate for efficient acidic water oxidation. *Sci. Adv.* 2023, 9 (42), No. eadi8025.
- (33) Huang, J.; Zhong, S.; Dai, Y.; Liu, C. C.; Zhang, H. Effect of MnO₂ Phase Structure on the Oxidative Reactivity toward Bisphenol A Degradation. *Environ. Sci. Technol.* **2018**, *52* (19), 11309–11318.
- (34) Peng, X.; Guo, Y.; Yin, Q.; Wu, J.; Zhao, J.; Wang, C.; Tao, S.; Chu, W.; Wu, C.; Xie, Y. Double-Exchange Effect in Two-Dimensional MnO₂ Nanomaterials. *J. Am. Chem. Soc.* **2017**, 139 (14), 5242–5248.
- (35) Yan, X.; Gan, T.; Shi, S.; Du, J.; Xu, G.; Zhang, W.; Yan, W.; Zou, Y.; Liu, G. Potassium-incorporated manganese oxide enhances the activity and durability of platinum catalysts for low-temperature CO oxidation. *Catal. Sci. Technol.* **2021**, *11* (19), 6369–6373.
- (36) Zheng, B.; Liu, G.; Geng, L.; Cui, J.; Wu, S.; Wu, P.; Jia, M.; Yan, W.; Zhang, W. Role of the FeO_x support in constructing high-performance Pt/FeO_x catalysts for low-temperature CO oxidation. *Catal. Sci. Technol.* **2016**, *6* (5), 1546–1554.
- (37) Muravev, V.; Spezzati, G.; Su, Y.-Q.; Parastaev, A.; Chiang, F.-K.; Longo, A.; Escudero, C.; Kosinov, N.; Hensen, E. J. M. Interface dynamics of Pd-CeO₂ single-atom catalysts during CO oxidation. *Nat. Catal.* **2021**, *4* (6), 469–478.
- (38) Lu, Y.; Wang, J.; Yu, L.; Kovarik, L.; Zhang, X.; Hoffman, A. S.; Gallo, A.; Bare, S. R.; Sokaras, D.; Kroll, T.; et al. Identification of the active complex for CO oxidation over single-atom Ir-on-MgAl₂O₄ catalysts. *Nat. Catal.* **2019**, 2 (2), 149–156.
- (39) Kühne, T. D.; Iannuzzi, M.; Del Ben, M.; Rybkin, V. V.; Seewald, P.; Stein, F.; Laino, T.; Khaliullin, R. Z.; Schütt, O.; Schiffmann, F.; Golze, D.; Wilhelm, J.; Chulkov, S.; Bani-Hashemian, M. H.; Weber, V.; Borštnik, U.; Taillefumier, M.; Jakobovits, A. S.;

- Lazzaro, A.; Pabst, H.; Müller, T.; Schade, R.; Guidon, M.; Andermatt, S.; Holmberg, N.; Schenter, G. K.; Hehn, A.; Bussy, A.; Belleflamme, F.; Tabacchi, G.; Glöß, A.; Lass, M.; Bethune, I.; Mundy, C. J.; Plessl, C.; Watkins, M.; VandeVondele, J.; Krack, M.; Hutter, J. CP2K: An electronic structure and molecular dynamics software package—Quickstep: Efficient and accurate electronic structure calculations. *J. Chem. Phys.* **2020**, *152*, 194103.
- (40) Giannozzi, P.; Baseggio, O.; Bonfa, P.; Brunato, D.; Car, R.; Carnimeo, I.; Cavazzoni, C.; de Gironcoli, S.; Delugas, P.; Ferrari Ruffino, F.; Ferretti, A.; Marzari, N.; Timrov, I.; Urru, A.; Baroni, S. Quantum ESPRESSO toward the exascale. *J. Chem. Phys.* **2020**, *152*, 154105.
- (41) Giannozzi, P.; Andreussi, O.; Brumme, T.; Bunau, O.; Buongiorno Nardelli, M.; Calandra, M.; Car, R.; Cavazzoni, C.; Ceresoli, D.; Cococcioni, M.; Colonna, N.; Carnimeo, I.; Dal Corso, A.; de Gironcoli, S.; Delugas, P.; DiStasio, R. A.; Ferretti, A.; Floris, A.; Fratesi, G.; Fugallo, G.; Gebauer, R.; Gerstmann, U.; Giustino, F.; Gorni, T.; Jia, J.; Kawamura, M.; Ko, H. Y.; Kokalj, A.; Küçükbenli, E.; Lazzeri, M.; Marsili, M.; Marzari, N.; Mauri, F.; Nguyen, N. L.; Nguyen, H. V.; Otero-de-la-Roza, A.; Paulatto, L.; Poncé, S.; Rocca, D.; Sabatini, R.; Santra, B.; Schlipf, M.; Seitsonen, A. P.; Smogunov, A.; Timrov, I.; Thonhauser, T.; Umari, P.; Vast, N.; Wu, X.; Baroni, S. Advanced capabilities for materials modelling with Quantum ESPRESSO. J. Phys. Condens. Matter 2017, 29, 465901.
- (42) Lu, T.; Chen, F. Multiwfn: A multifunctional wavefunction analyzer. *J. Comput. Chem.* **2012**, *33*, 580–592.
- (43) Maintz, S.; Deringer, V. L.; Tchougréeff, A. L.; Dronskowski, R. LOBSTER: A tool to extract chemical bonding from plane-wave based DFT. *J. Comput. Chem.* **2016**, *37*, 1030–1035.
- (44) Momma, K.; Izumi, F. VESTA 3 for three-dimensional visualization of crystal, volumetric and morphology data. *J. Appl. Crystallogr.* **2011**, *44*, 1272–1276.
- (45) Mansouri, M. Effects of Vacancy-Defected, Dopant and the Adsorption of Water upon Mn₂O₃ and Mn₃O₄ (001) Surfaces: A First-Principles Study. *Acta Phys. Pol.*, A **2018**, 133, 1178–1185.
- (46) Bridgeman, A. J.; Cavigliasso, G.; Ireland, L. R.; Rothery, J. The Mayer bond order as a tool in inorganic chemistry. *Dalton Trans.* **2001**, 2095–2108.
- (47) Mayer, I. Charge, bond order and valence in the AB initio SCF theory. *Chem. Phys. Lett.* **1983**, *97*, 270–274.
- (48) Dronskowski, R.; Bloechl, P. E. Crystal orbital Hamilton populations (COHP): energy-resolved visualization of chemical bonding in solids based on density-functional calculations. *J. Phys. Chem.* **1993**, 97, 8617–8624.
- (49) Deringer, V. L.; Tchougréeff, A. L.; Dronskowski, R. Crystal Orbital Hamilton Population (COHP) Analysis As Projected from Plane-Wave Basis Sets. *J. Phys. Chem. A* **2011**, *115*, 5461–5466.
- (50) Yan, H.; Shen, Q.; Sun, Y.; Zhao, S.; Lu, R.; Gong, M.; Liu, Y.; Zhou, X.; Jin, X.; Feng, X.; Chen, X.; Chen, D.; Yang, C. Tailoring Facets of α -Mn₂O₃ Microcrystalline Catalysts for Enhanced Selective Oxidation of Glycerol to Glycolic Acid. *ACS Catal.* **2021**, *11*, 6371–6383.